PNAS RESEARCH ARTICLE | DEVELOPMENTAL BIOLOGY
BIOPHYSICS AND COMPUTATIONAL BIOLOGY OPEN ACCESS

Allosteric inhibition of the IZUMO1–JUNO fertilization complex by the naturally occurring antisperm antibody OBF13

Yonggang Lu[a,b], Masahito Ikawa[b,c,d,e], and Shaogeng Tang[f,1]

Edited by Mariana Wolfner, Cornell University, Ithaca, NY; received December 18, 2024; accepted February 5, 2025

Sperm IZUMO1 binds to egg JUNO, and this interaction is essential for mammalian fertilization. Isolated from a female mouse immunized with syngeneic sperm, the antisperm antibody OBF13 recognizes IZUMO1 and inhibits murine fertilization. How OBF13 interferes with sperm–egg interactions was unknown. Here, we present the X-ray crystal structure of IZUMO1 in complex with OBF13. OBF13 binds to the apex of the four-helix domain of IZUMO1, distant from the JUNO-binding site. Our crystal structure of OBF13-bound IZUMO1 resembles apo-IZUMO1 and differs from the structure of IZUMO1 in complex with JUNO. We identify that OBF13 carries a low level of somatic hypermutation, and through deep mutational scanning, we engineer an affinity-enhanced OBF13 variant. This OBF13 variant single-chain fragment variable decreases the apparent affinity of IZUMO1 for membrane-bound murine JUNO and blocks the binding of acrosome-reacted sperm to eggs, thereby preventing fertilization. We propose allostery between the OBF13 epitope and the JUNO-binding site. OBF13 inhibits a conformational change in IZUMO1, preventing fusion-competent sperm from adhering to murine eggs during fertilization. Surprisingly, murine IZUMO1 binds to hamster JUNO with an affinity ~20-fold higher than to murine JUNO. The decreased affinity caused by OBF13 of murine IZUMO1 for hamster JUNO is sufficient for murine sperm to bind to and fuse with hamster eggs. Our studies provide a structural and mechanistic framework for species-specific, allosteric inhibition of IZUMO1 by a naturally occurring antisperm antibody and offer insights into the development of immunocontraceptives.

fertilization | antisperm antibody | IZUMO1 | infertility | contraception

Significance

In the United States, 9% of men and 11% of women of reproductive age experience fertility problems. Successful fertilization requires the proper recognition, adhesion, and fusion of sperm and an egg. Here, we show how a naturally occurring antisperm antibody OBF13, which targets sperm IZUMO1, can block murine fertilization. We provide structural and molecular mechanisms how OBF13 inhibits a critical conformational change of IZUMO1 and interferes with the IZUMO1–JUNO fertilization complex when sperm interact with eggs. Our findings suggest avenues for the diagnosis and treatment of immuno-infertility, as well as the development of immunocontraceptives.

Fertilization is a central event of sexual reproduction, facilitated by critical gamete-surface interactions between sperm IZUMO1 and egg JUNO (1, 2). Several sperm proteins, including SPACA6, TMEM81, FIMP, TMEM95, DCST1, DCST2, and SOF1, have been identified as essential factors in mammalian sperm–egg interactions (3–12). First isolated in the 1980s (13), the antisperm antibody, OBF13 (Okabe, Butsu-Metsu, Friday the 13th), led to the discovery of sperm IZUMO1 (1). Secreted by a hybridoma originating from a female mouse immunized with syngeneic murine sperm, OBF13 recognizes the sperm heads that have undergone the acrosome reactions (14, 15). When zona pellucida is removed, murine sperm can fuse with murine and hamster eggs in vitro. It was observed that OBF13 inhibits murine sperm from fertilizing murine eggs, but not hamster eggs (16, 17).

In this study, motivated by the hypothesis that OBF13 recognizes a specific, fertilization-inhibitory epitope of sperm IZUMO1, we determined the X-ray crystal structures of the murine IZUMO1 ectodomain in complex with the fragment antigen-binding (Fab) region of OBF13, as well as apo-IZUMO1. OBF13 targets the apex of the four-helix domain of IZUMO1, and remarkably, this interaction does not overlap with the JUNO-binding site. Analyses of our structures revealed that the boomerang-shaped apo-IZUMO1 changes conformation when forming a complex with JUNO. Therefore, OBF13 targeting the apex of IZUMO1 could have an allosteric effect for JUNO binding.

We found that OBF13 prevents the adhesion of murine sperm to eggs in vitro, independent of antibody size. Using deep mutational scanning and yeast surface display, we selected paratope variants of OBF13 with enhanced IZUMO1 binding. We identified a quintuple variant single-chain fragments variable (scFv) of OBF13, termed high-affinity consensus (HAC). This small, 25 kDa variant binds IZUMO1 with nanomolar affinity. We observed that both OBF13 (IgM) and OBF13^{HAC} (scFv) similarly decrease the interactions between a bivalent IZUMO1 ectodomain and cell surface-bound murine JUNO and inhibit the binding of acrosome-reacted sperm to zona-free murine eggs, thereby blocking fertilization in vitro.

Author affiliations: [a]Premium Research Institute for Human Metaverse Medicine, Osaka University, Suita, Osaka 565-0871, Japan; [b]Research Institute for Microbial Diseases, Osaka University, Suita, Osaka 565-0871, Japan; [c]The Institute of Medical Science, The University of Tokyo, Minato-ku, Tokyo 108-8639, Japan; [d]Center for Infectious Disease Education and Research, Osaka University, Suita, Osaka 565-0871, Japan; [e]Center for Advanced Modalities and Drug Delivery System, Osaka University, Suita, Osaka 565-0871, Japan; and [f]Department of Molecular Biophysics and Biochemistry, Yale University, New Haven, CT 06520

Author contributions: Y.L., M.I., and S.T. designed research; performed research; contributed new reagents/analytic tools; analyzed data; and wrote the paper.

The authors declare no competing interest.

This article is a PNAS Direct Submission.

Copyright © 2025 the Author(s). Published by PNAS. This open access article is distributed under Creative Commons Attribution-NonCommercial-NoDerivatives License 4.0 (CC BY-NC-ND).

[1]To whom correspondence may be addressed. Email: shaogeng.tang@yale.edu.

This article contains supporting information online at https://www.pnas.org/lookup/suppl/doi:10.1073/pnas.2425952122/-/DCSupplemental.

Published March 5, 2025.

Counterintuitively, we found that murine IZUMO1 binds more strongly to hamster JUNO than to murine JUNO. Using structure-based site-directed mutagenesis, we identified key amino acid sites on JUNO that define its IZUMO1-binding affinity. Despite both OBF13 (IgM) and OBF13^{HAC} (scFv) modestly affecting the binding of IZUMO1 to hamster JUNO, the resulting affinities remain sufficient for the binding of murine sperm to hamster eggs during fertilization. Taken together, our studies on the antisperm antibody OBF13 suggest allosteric regulation of IZUMO1-mediated sperm–egg interactions and inform the design and development of immuno-contraceptives.

Results

OBF13 Recognizes the Apex of the Four-Helix Domain of IZUMO1. We hypothesized that OBF13 recognizes a conformational epitope within the IZUMO1 ectodomain that is important for fertilization (18). To characterize how OBF13 binds to IZUMO1, we first obtained the antibody coding sequences from the OBF13 hybridoma. As a murine IgM with a Kappa light chain (*SI Appendix*, Fig. S1*A*), OBF13 belongs to the lineages carrying IGHV14-3*02 and IGKV6-15*01 gene segments with low somatic mutations showing 99.0 and 97.9% identities to the heavy and light chain germline sequences, respectively (*SI Appendix*, Fig. S1 *D*–*G* and Table S2).

To obtain the IZUMO1–OBF13 complex to homogeneity, we recombinantly expressed and purified the ectodomain of IZUMO1 and constructed the Fab region of OBF13 (Fig. 1*A* and *SI Appendix*, Fig. S1 *B* and *C*). We determined an X-ray cocrystal structure of the antigen–antibody complex at 3.1 Å resolution (Fig. 1*B*). The crystal belongs to space group *P* 1, containing two IZUMO1–OBF13 complexes per asymmetric unit, which adopt a similar overall architecture with a C_α rmsd of 0.64 Å (*SI Appendix*, Fig. S2*H*). The complementary determining regions (CDRs) of the heavy and light chains of OBF13 interact with the apex of the four-helix domain of IZUMO1 (Fig. 1*C*). The epitope is composed of the N-termini of the α2 and α4 helices, as well as the α1-α2 and α3-α4 loops of IZUMO1 (Fig. 1*C*), spanning 904.7 Å^2 solvent-accessible surface area.

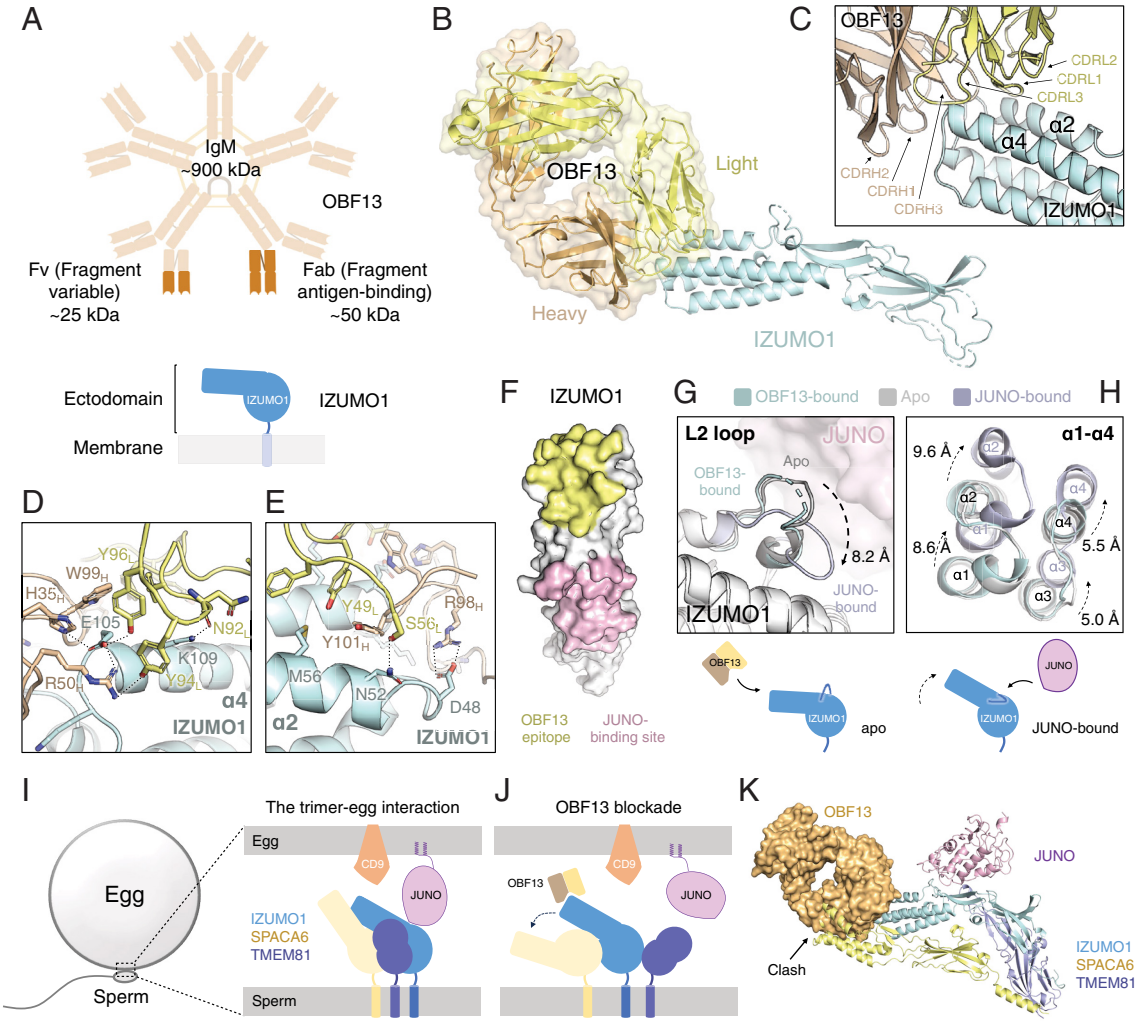

Fig. 1. OBF13 recognizes the apex of the four-helix domain of IZUMO1. (*A*) Cartoon schematics of IgM, Fab, and Fv of OBF13 and IZUMO1. (*B*) Ribbon diagram of the X-ray crystal structure of IZUMO1–OBF13. The heavy chain of OBF13 in light orange, the light chain in pale yellow, and IZUMO1 in pale cyan. (*C*) A close-up view of the IZUMO1–OBF13 interface, with the α2 and α4 helices of IZUMO1 and the CDR loops of OBF13 labeled. Close-up views of OBF13 paratope interacting with the (*D*) α4 and (*E*) α2 helices of IZUMO1. Dash lines representing hydrogen bonds and salt bridges. (*F*) Space-filling model of IZUMO1 ectodomain. The OBF13 epitope is in pale yellow and the JUNO-binding site in light pink. Close-up views of overlaid IZUMO1 from the OBF13-bound (pale cyan), apo (light gray), and JUNO-bound (blue-white) structures showing the conformational differences in (*G*) the L2 loop and (*H*) the four-helix domain. Cartoon models showing that (*Left*) OBF13 recognizes the apex of the four-helix domain of IZUMO1 in IZUMO1's apo conformation and (*Right*) the four-helix domain moves up and the L2 loop moves down when IZUMO1 binds to JUNO. Cartoon schematics showing (*I*) the sperm IZUMO1–SPACA6–TMEM81 complex and egg JUNO and CD9, and (*J*) OBF13-depedent disruption of the IZUMO1–SPACA6–TMEM81 complex formation. (*K*) Structural overlay of an AlphaFold predicted sperm IZUMO1–SPACA6–TMEM81 complex and egg JUNO with the IZUMO1–OBF13 complex, showing that OBF13 makes a clash with SPACA6 when OBF13 interacts with IZUMO1.

We found that OBF13 and JUNO bind to two nonoverlapping surfaces of IZUMO1 (Fig. 1*F*). By overlaying our IZUMO1–OBF13 structure with the previously determined human IZUMO1–JUNO structures (19, 20), we observed conformational changes within IZUMO1. Upon binding JUNO, an 8.2 Å shift occurs in the L2 loop of IZUMO1 (Fig. 1*G*). This conformational change rearranges the surface of the rear end of the four-helix domain and the β-hairpin hinge region to accommodate JUNO binding. These rearrangements propagate to the front end of the four-helix domain, resulting in a remarkable ~9 Å upward shift of the OBF13 epitope (Fig. 1*H*).

OBF13 was elicited against IZUMO1 expressed on murine sperm (13) and, therefore, recognizes the conformation of apo-IZUMO1 (Fig. 1*A*). To assist in analyzing the conformational changes in IZUMO1 associated with OBF13 and JUNO binding, we determined an X-ray crystal structure of apo-IZUMO1 at 1.8 Å resolution. Similar to a previously determined IZUMO1 structure (21), the crystal contains a single IZUMO1 molecule per asymmetric unit, with space group *I* 422 (*SI Appendix*, Fig. S2 *A–G*). We superimposed our apo and OBF13-bound structures of IZUMO1 and found that two structures have similar conformations of four-helix domain and the L2 loop, with an overall C_α (rmsd) of 0.69 Å (Fig. 1 *G* and *H* and *SI Appendix*, Fig. S2 *I–K*).

We note that the OBF13 epitope overlaps with the predicted Bouncer-binding site of the IZUMO1–SPACA6–TMEM81 complex in zebrafish (12). Such trimeric sperm complex is predicted by AlphaFold in mammals (11, 12) (Fig. 1*I*) and OBF13 binding would disrupt the heterotrimer formation (Fig. 1 *J* and *K*). We also note that the overall change is more dramatic in human IZUMO1 (19). Upon binding human JUNO, a 12 Å shift in the L2 loop and a 20 Å shift of the apex of the four-helix domain occurs, changing IZUMO1 from the boomerang conformation to the upright conformation (*SI Appendix*, Fig. S2*L*). Taken together, our results provide a structural basis for systematic rearrangements of IZUMO1 that couple the four-helix domain movement and change of the L2 loop when IZUMO1 binds OBF13 or JUNO.

Engineering OBF13 Variants with Enhanced IZUMO1 Affinity. Because the bulkiness of IgM has steric effects (Fig. 1*A*), we sought to evaluate whether OBF13's single-chain fragment variable (scFv), which has a much-reduced size, exhibits a similar effect on IZUMO1 activity. Using biolayer interferometry (BLI), we found that IZUMO1 binds OBF13 scFv with a modest affinity, with a K_D of 1.0 μM, largely due to the fast dissociation rate constant (k_{off}) (Fig. 2*F* and *SI Appendix*, Fig. S1*G*). We postulated that the fast off-rate of OBF13 scFv would be insufficient for small, monomeric antigen-binding domains to stabilize the apo-IZUMO1 conformation on sperm.

We hypothesized that amino acid substitutions on the paratope (Fig. 2*A*) could decrease the dissociation rate constant and increase the binding affinity between OBF13 and IZUMO1. To test this, we performed structure-based deep mutational scanning (22, 23) to construct an OBF13 variant library with trinucleotides encoding all 20 possible amino acids at each position of the OBF13 paratope. We then used yeast surface display (24, 25) of OBF13 scFv with a recombinant murine IZUMO1-human Fc fusion protein (9, 26) as the selection agent (Fig. 2*B* and *SI Appendix*, Fig. S3*A*). After magnetic- and fluorescence-activated cell sorting, we isolated OBF13 variant clones with single-residue substitutions (Fig. 2*C* and *SI Appendix*, Fig. S3*B*). Substitutions were identified at two positions in the heavy chain (D31Q in CDRH1 and Y104W in CDRH3) and three positions in the light chain (T31W in CDRL1, Y49F, and S56P in CDRL2) (Fig. 2*D* and *SI Appendix*, Fig. S3 *C* and *D*).

To obtain a high-affinity OBF13 variant, we combined all five amino acid substitutions. While the wild-type (WT) OBF13 scFv binds to IZUMO1-Fc with an EC_{50} of 40.8 nM on yeast surface display, the quintuple variant showed a drastically increased apparent affinity with an EC_{50} of 442 pM (Fig. 2*E*). To validate the detected enhancement in affinity, we recombinantly expressed and purified the OBF13 paratope variants. Using BLI, all variants exhibited increased IZUMO1 affinity. Remarkably, the OBF13 quintuple variant had a K_D of 7.9 nM for IZUMO1 (Fig. 2*F* and *SI Appendix*, Fig. S3 *E* and *F*), which we hereafter refer to as OBF13 high-affinity consensus (HAC).

We note that OBF13 carries only three amino acid substitutions (one in variable heavy domain, V_H, and one in variable light domain, V_L) from its inferred germline antibody (*SI Appendix*, Fig. S3*I*), which can bind IZUMO1 with a K_D of 7.0 μM (*SI Appendix*, Fig. S3 *G* and *H*). By immunization of sperm, these lineages of OBF13 underwent somatic hypermutations in vivo, resulting in a sevenfold improvement in affinity. In our study, $OBF13^{HAC}$ received an additional 126-fold improvement through directed affinity maturation in vitro. $OBF13^{HAC}$ carries a total of eight amino acid substitutions (three in V_H and five in V_L) from its inferred germline, constituting an 886-fold increase in affinity for IZUMO1 (Fig. 2*G*).

$OBF13^{HAC}$ Decreases the Affinity and Association Kinetics for the Binding of IZUMO1 to Murine JUNO. We next examined whether $OBF13^{HAC}$ affects the IZUMO1–JUNO interaction. Using BLI, we compared the binding to murine JUNO in solution with sensor-loaded IZUMO1-Fc. WT IZUMO1 binds murine JUNO with a K_D of 11 μM. When IZUMO1 was prebound to $OBF13^{HAC}$ (scFv) or OBF13 (IgM) (Fig. 3*A*), it exhibited decreased murine JUNO affinity, with K_D values of 33.8 μM and 30.1 μM, respectively (Fig. 3*B* and *SI Appendix*, Fig. S4 *A–C*). Compared to IZUMO1 alone, the antibody-bound IZUMO1 showed a threefold decrease in the association rate constant (k_{on}) for murine JUNO (Fig. 3*B*). These results suggest that $OBF13^{HAC}$ (scFv) or OBF13 (IgM) recognize conformational ensembles of apo-IZUMO1 different from its JUNO-bound state.

We then evaluated whether $OBF13^{HAC}$ affects the binding of the IZUMO1 ectodomain to membrane-bound JUNO on the cell surface. To do this, we transfected HEK293F cells to ectopically express glycosylphosphatidylinositol (GPI)-anchored murine JUNO and incubated live cells with a serial dilution of defined concentrations of IZUMO1-Fc. Using an AlexaFluor647-conjugated anti-Fc antibody, we recorded the percentages of AlexaFluor647-positive cells for each concentration of IZUMO1-Fc (Fig. 3*C*). While IZUMO1-Fc had an EC_{50} of 10.7 nM to murine JUNO on the cell surface, IZUMO1-Fc prebound to $OBF13^{HAC}$ (scFv) or OBF13 (IgM) showed a ~50-fold decrease in apparent affinity, with EC_{50} values of 557 nM and 551 nM, respectively (Fig. 3*D*). Despite HEK293F cells express CD9, we did not detect binding of IZUMO1-Fc to HEK293F cells that are not transfected with JUNO (*SI Appendix*, Fig. S4*D*). The subtle effects observed in in-solution measurements become more pronounced when tested at enhanced avidity on the cell surface.

We found that $OBF13^{HAC}$ inhibits the binding of IZUMO1-Fc to murine egg's plasma membranes. When incubated with zona-free eggs, IZUMO1-Fc binds to WT eggs but not to *Juno* knock-out eggs (*SI Appendix*, Fig. S4*E*). However, when 100 nM IZUMO1-Fc is prebound to $OBF13^{HAC}$ (scFv) or OBF13 (IgM), we observed drastically reduced egg-binding activities compared to IZUMO1-Fc alone and IZUMO1-Fc prebound to WT OBF13 (scFv) (*SI Appendix*, Fig. S4 *F* and *G*). Collectively, these results suggest that independent from antibody's size, a high-affinity

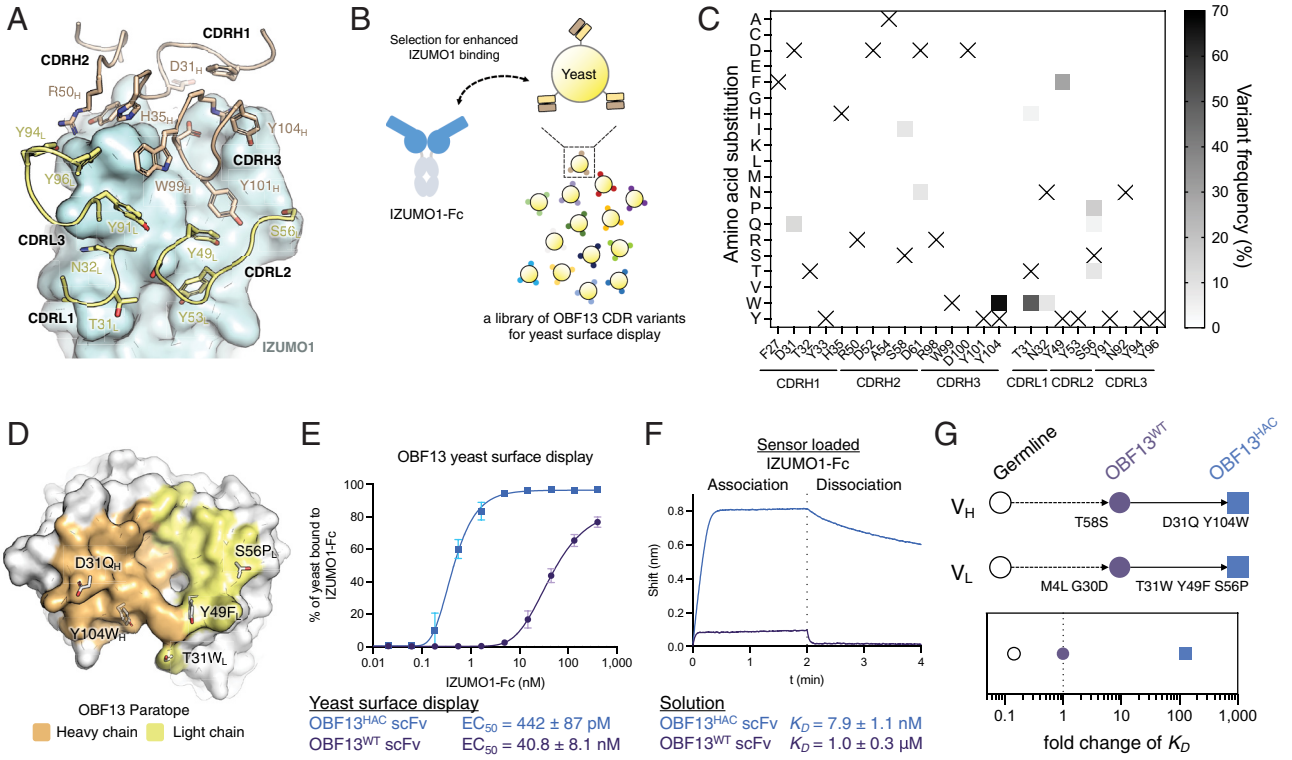

Fig. 2. Engineering OBF13 variants with enhanced IZUMO1 affinity. (*A*) Structure of the OBF13 paratope with the CDR loops of the heavy and light chains in ribbon diagrams and IZUMO1 epitope in a space-filling model. The heavy chain of OBF13 in light orange, the light chain in pale yellow, and IZUMO1 in pale cyan. (*B*) Schematic of yeast surface display of the OBF13 CDR variant library (colored spheres) and selection for binding of a recombinant IZUMO1-Fc protein. (*C*) Summary of deep mutational scanning shown in a frequency heatmap of OBF13 CDR variants after selection round 3 of the yeast surface display selection using IZUMO1-Fc. Substitutions of D31Q and Y104W were identified in the heavy chain and T31W, Y49F, and S56P in the light chain. (*D*) A space-filling model of the OBF13 paratope with the heavy chain of OBF13 in light orange and the light chain in pale yellow. Side chains of the amino acid substitutions showing increased affinity for IZUMO1 found in (*C*) were labeled. (*E*) Titration curves of yeast surface displayed OBF13^{WT} scFv (dark purple) and OBF13^{HAC} scFv (blue) labeled with a serial dilution of IZUMO1-Fc, followed by AlexaFluor647-conjugated anti-Fc antibody. Fitting was performed in Graphpad Prism 10. Means and SD were calculated from three independent measurements. (*F*) Biolayer interferometric traces showing binding of sensor-loaded IZUMO1 to 333 nM OBF13^{WT} scFv (dark purple) or 333 nM OBF13^{HAC} scFv (blue) in solution. (*G*) Schematics of antibody evolution of variable heavy (V_H) and variable light (V_L) from germline, to OBF13^{WT}, and to OBF13^{HAC}. Summary of fold changes of K_D of IZUMO1-Fc to the antibody.

OBF13^{HAC} (scFv) or a high-avidity OBF13 (IgM) decreases the binding of IZUMO1 to membrane-bound murine JUNO.

OBF13^{HAC} Inhibits Acrosome-Reacted Murine Sperm From Adhering to Murine Eggs. It was established that OBF13 (IgM) potently inhibits murine sperm to fertilize murine eggs. We hypothesized that the altered affinity caused by OBF13 between sperm IZUMO1 and egg JUNO inhibits murine sperm–egg binding during fertilization. Since both acrosome-reacted and acrosome-intact murine sperm can bind to zona-free murine eggs in vitro (27), we chose to employ red body green sperm (RBGS) male mice (28). Sperm from these mice express EGFP-tagged Acrosin, a soluble acrosomal protein rapidly released during acrosome reaction, allowing for direct visualization by green fluorescence to distinguish the acrosomal status of each sperm (Fig. 3*E*).

We incubated zona-free murine eggs with capacitated sperm pretreated with the antibodies. 30 min after insemination, we recorded the number of acrosome-reacted sperm, indicated by the loss of green fluorescence in the sperm head, bound to eggs. Compared to the untreated group, the OBF13^{HAC} (scFv)- and OBF13 (IgM)-treated groups had drastically reduced binding activity (Fig. 3 *F* and *G*). 6 h after insemination, we recorded the number of pronuclei per egg. In the untreated group, there were approximately 3.5 fused sperm per egg. However, no sperm–egg fusion was detected in the OBF13^{HAC} (scFv)- and OBF13 (IgM)-treated groups. The WT OBF13 (scFv) had minimal effect on sperm–egg binding or fusion (Fig. 3 *F* and *G* and *SI Appendix*, Fig. S4 *H* and *I*). These results suggest that, independent from antibody's size, the binding of high-affinity OBF13^{HAC} (scFv) or high-avidity OBF13 (IgM) to sperm inhibits the adhesion of fusion-competent sperm to eggs, thereby preventing membrane fusion during in vitro fertilization.

Murine IZUMO1 Binds Strongly to Hamster JUNO. Although it was known that murine IZUMO1 can bind to hamster JUNO (29), we were intrigued that OBF13 (IgM) selectively allows for murine sperm to fertilize hamster eggs (16). Surprisingly, we found that the interaction of murine IZUMO1 with hamster JUNO in solution has a K_D of 659.3 nM, 20-fold higher than the K_D for murine IZUMO1 with murine JUNO (Fig. 4*A* and *SI Appendix*, Fig. S5*A*). To better understand the affinities, we next analyzed the surface of JUNO that interacts with IZUMO1 (30). We found that while the interfacial amino acids between murine and hamster JUNO are mostly conserved, five amino acid sites differ (Y44, Q45, R58, R87, and L141 of murine JUNO) (Fig. 4*B* and *SI Appendix*, Fig. S5*B*). We postulated that these five sites contain the determinants for the affinity enhancement. To test this, we performed site-directed mutagenesis on murine JUNO to substitute the amino acids with those from the hamster sequence. Using BLI, we found that, compared to WT JUNO, Q45L has minimal effects, Y44F completely ablates the binding, and R58F, R87H, and L141Y exhibit increased affinity. Remarkably, L141Y alone is sufficient to boost the affinity to the

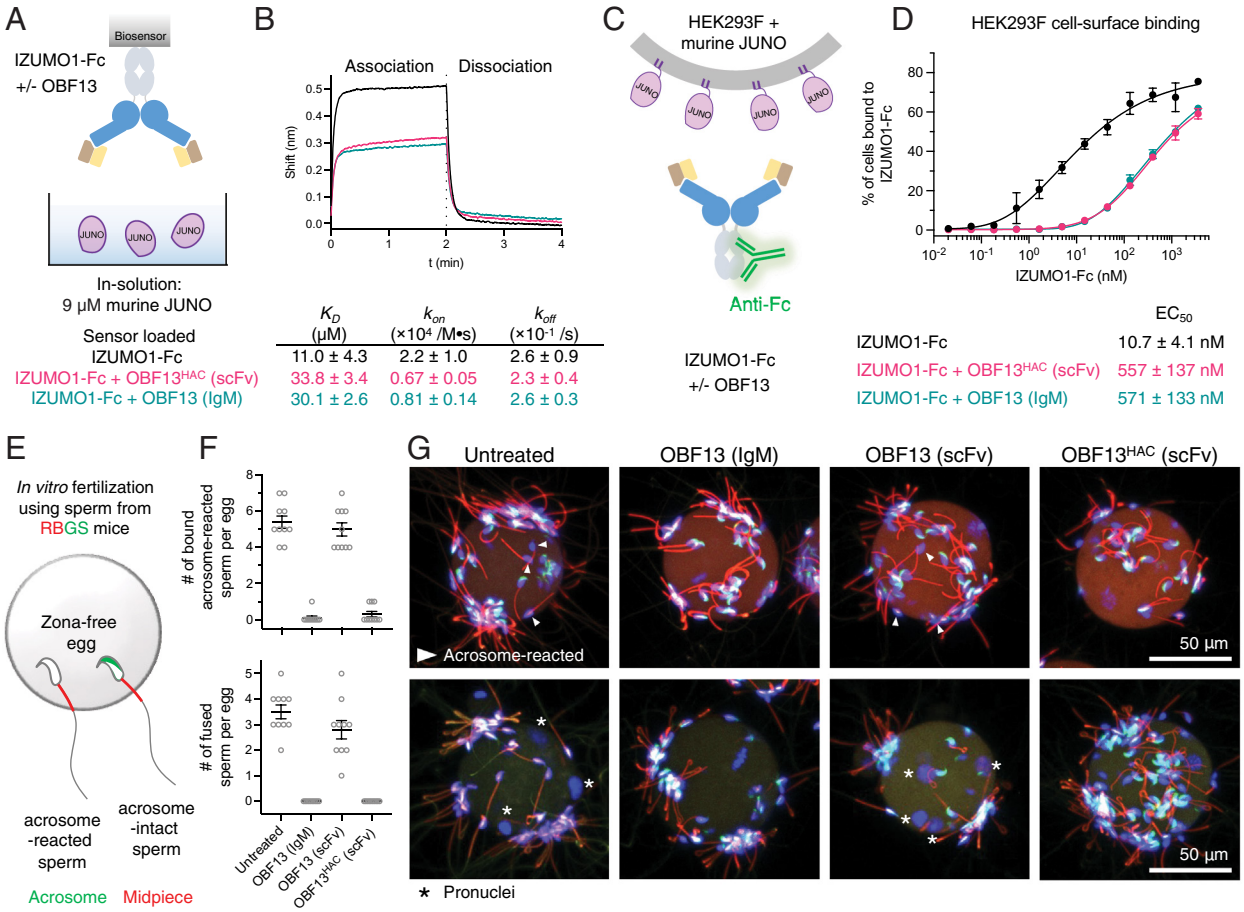

	K_D (μM)	k_{on} (×10⁴ /M•s)	k_{off} (×10⁻¹ /s)
Sensor loaded IZUMO1-Fc	11.0 ± 4.3	2.2 ± 1.0	2.6 ± 0.9
IZUMO1-Fc + OBF13^{HAC} (scFv)	33.8 ± 3.4	0.67 ± 0.05	2.3 ± 0.4
IZUMO1-Fc + OBF13 (IgM)	30.1 ± 2.6	0.81 ± 0.14	2.6 ± 0.3

	EC_{50}
IZUMO1-Fc	10.7 ± 4.1 nM
IZUMO1-Fc + OBF13^{HAC} (scFv)	557 ± 137 nM
IZUMO1-Fc + OBF13 (IgM)	571 ± 133 nM

Fig. 3. OBF13^{HAC} inhibits acrosome-reacted sperm from adhering to murine eggs. (*A*) Cartoon schematics showing (*B*) the BLI experiments using sensor-loaded IZUMO1-Fc alone, or IZUMO1-Fc in complex with OBF13^{HAC} (scFv) or OBF13 (IgM), binding to 9 μM murine JUNO ectodomain in solution. (*C*) Cartoon schematics showing (*D*) the flow cytometric experiments using HEK293F expressing cell-surface, GPI-anchored murine JUNO labeled with a serial dilution of IZUMO1-Fc and an AlexaFluor647-conjugated anti-Fc antibody. (*E*) Cartoon schematic showing the in vitro fertilization experiment using sperm from RBGS mice and WT eggs. Acrosome-intact sperm have green fluorescence from Acrosin-GFP in the sperm head; acrosome-reacted sperm lose the green fluorescence. (*F*) Summary of (*Upper*) the numbers of bound acrosome-reacted murine RBGS sperm per zona-free murine eggs (mean ± SEM), untreated 5.4 ± 0.3 (N = 10), OBF13 (IgM)-treated 0.1 ± 0.1 (N = 10), OBF13^{WT} (scFv)-treated 5.0 ± 0.4 (N = 10), and OBF13^{HAC} (scFv)-treated 0.3 ± 0.2 (N = 10), and (*Lower*) the numbers of fused RBGS sperm per zona-free murine eggs (mean ± SEM), untreated 3.5 ± 0.3 (N = 10), OBF13 (IgM)-treated 0 ± 0 (N = 10), OBF13^{WT} (scFv)-treated 2.8 ± 0.4 (N = 10), and OBF13^{HAC} (scFv)-treated 0 ± 0 (N = 10). (*G*) Representative z-stack confocal micrographs of the four groups in (*F*) showing (upper) 30 min after insemination, binding of murine RBGS sperm to zona-free murine eggs, and (*Lower*) 6 h after insemination, the formation of pronuclei inside zona-free murine eggs. Acrosome by Acrosin-EGFP in green, Mitochondria in midpiece by CAG/Su9-DsRed2 in red, and nuclei by Hoechst 33342 in blue. (Scale bar, 50 μm.)

level of hamster JUNO (Fig. 4*C*). These results suggested that the amino acid difference at position 141 from leucine to tyrosine is a predominant determinant for murine IZUMO1 binding more strongly to hamster JUNO than to murine JUNO.

We examined whether OBF13^{HAC} affects the murine IZUMO1–hamster JUNO interaction. Using BLI, we compared the binding to hamster JUNO in solution with sensor-loaded IZUMO1-Fc prebound to the antibodies (Fig. 4*D*). Compared to IZUMO1 alone, the OBF13^{HAC} (scFv)- or OBF13 (IgM)-bound IZUMO1 showed a twofold decrease in k_{on} for hamster JUNO (Fig. 4*E* and *SI Appendix*, Fig. S5 *C–E*), suggesting that the antibodies preferably recognize a conformation of apo-IZUMO1 different from that bound to hamster JUNO. Because antibody binding also alters k_{off}, the resulting K_D has minimal change. When binding to membrane-bound hamster JUNO on the HEK293F cell surface (Fig. 4*F*), IZUMO1-Fc exhibits an EC_{50} of 198 pM. However, when IZUMO1-Fc is prebound to OBF13^{HAC} (scFv) or OBF13 (IgM), there is a decrease in its apparent affinity with EC_{50} values of 785 pM and 1,404 pM, respectively (Fig. 4*G*). Despite decrease in binding, the resulting EC_{50} values are lower than the EC_{50} for IZUMO1-Fc binding to murine JUNO on the cell surface (Fig. 4*G*). Therefore, we proposed that the altered affinity caused by the antibodies can sustain murine IZUMO1 to properly interact with hamster JUNO at the cell surface, allowing for sufficient sperm–egg interactions during fertilization.

OBF13^{HAC} Does Not Inhibit Murine Sperm from Fertilizing Hamster Eggs. We next evaluated OBF13^{HAC} on the ability of murine IZUMO1 to bind to and of murine sperm to fertilize hamster eggs. We found that when IZUMO1-Fc was incubated with hamster eggs, similar to OBF13 (IgM), OBF13^{HAC} (scFv) does not ablate the binding of IZUMO1-Fc to zona-free hamster eggs (*SI Appendix*, Fig. S5*F*). To evaluate fertilization, we next inseminated hamster eggs with murine sperm preincubated with WT OBF13 (scFv) and OBF13^{HAC} (scFv), using an untreated group and the OBF13 (IgM)-treated group as controls. We recorded the numbers of bound and fused sperm per egg and found that neither group blocks binding or fusion of murine sperm to hamster eggs (Fig. 4 *H–J*).

Because of the high affinity and high avidity of murine IZUMO1 to hamster JUNO at the cell surfaces, the affinity changes caused by OBF13^{HAC} (scFv) remain sufficient to enable murine sperm–hamster egg interactions during fertilization.

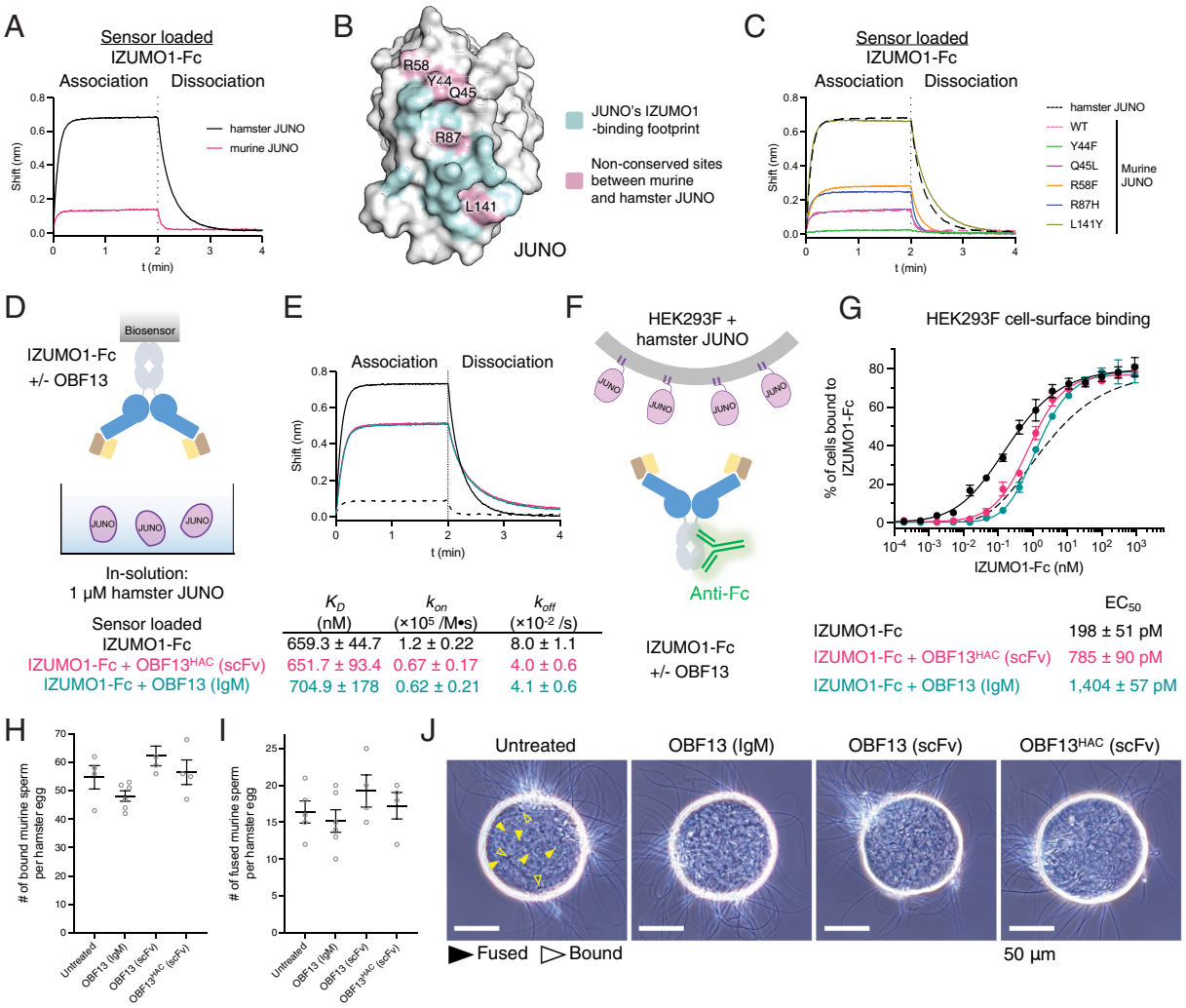

Sensor loaded IZUMO1-Fc	K_D (nM)	k_{on} ($\times 10^5$ /M•s)	k_{off} ($\times 10^{-2}$ /s)
IZUMO1-Fc	659.3 ± 44.7	1.2 ± 0.22	8.0 ± 1.1
IZUMO1-Fc + OBF13^{HAC} (scFv)	651.7 ± 93.4	0.67 ± 0.17	4.0 ± 0.6
IZUMO1-Fc + OBF13 (IgM)	704.9 ± 178	0.62 ± 0.21	4.1 ± 0.6

IZUMO1-Fc +/- OBF13	EC_{50}
IZUMO1-Fc	198 ± 51 pM
IZUMO1-Fc + OBF13^{HAC} (scFv)	785 ± 90 pM
IZUMO1-Fc + OBF13 (IgM)	1,404 ± 57 pM

Fig. 4. Murine IZUMO1 binds strongly to hamster JUNO. (*A*) Biolayer interferometric traces showing binding of sensor-loaded IZUMO1-Fc to 1 μM hamster JUNO (black) and 1 μM murine JUNO (red violet). Association for 2 min and dissociation for 2 min. (*B*) A space-filling of murine JUNO (PDB ID: 5EJN) with the IZUMO1-binding footprint in cyan and pink and the pink depicting residues that are different between murine and hamster JUNO. (*C*) Biolayer interferometric traces showing binding of sensor-loaded IZUMO1-Fc to 1 μM hamster JUNO (dash line) as a reference and 1 μM wildtype murine JUNO, or the Y44F, Q45L, R58F, R87H, L141Y murine JUNO variants. Association for 2 min and dissociation for 2 min. (*D*) Cartoon schematics showing (*E*) the BLI experiments using sensor-loaded IZUMO1-Fc alone, or IZUMO1-Fc in complex with OBF13^{HAC} (scFv) or OBF13 (IgM), binding to 1 μM hamster JUNO ectodomain in solution. (*F*) Cartoon schematics showing (*G*) the flow cytometric experiments using HEK293F expressing cell-surface, GPI-anchored hamster JUNO labeled with a serial dilution of IZUMO1-Fc and an AlexaFluor647-conjugated anti-Fc antibody. As a reference, the dash line represents the IZUMO1-Fc binding to HEK293F-expressed murine JUNO as shown in Fig. 3*D*. (*H*) Summary of the numbers of bound murine sperm per zona-free hamster eggs (mean ± SEM), untreated 54.8 ± 4.1 (N = 4), OBF13 (IgM)-treated 48.2 ± 1.9 (N = 6), OBF13^{WT} (scFv)-treated 62.3 ± 3.5 (N = 4), and OBF13^{HAC} (scFv)-treated 56.5 ± 4.3 (N = 4). (*I*) Summary of the numbers of fused murine sperm per zona-free hamster eggs (mean ± SEM), untreated 16.4 ± 1.5 (N = 5), OBF13 (IgM)-treated 15.2 ± 1.5 (N = 6), OBF13^{WT} (scFv)-treated 19.3 ± 2.2 (N = 6), and OBF13^{HAC} (scFv)-treated 17.3 ± 1.8 (N = 6). (*J*) Representative phase contrast micrographs of the four groups in (*H* and *I*) showing 3 h after insemination binding of murine sperm to zona-free hamster eggs. (Scale bar, 50 μm.)

Collectively, these results provided structural and biochemical basis for the species-selective inhibition of fertilization by OBF13.

Discussion

The antisperm antibody OBF13 targets the four-helix domain of IZUMO1 and inhibits IZUMO1-mediated sperm–egg binding before membrane fusion during fertilization. This inhibition is independent of antibody size, indicating that steric hindrance in membrane fusion does not impede the antibody's inhibition. An inferred germline antibody of OBF13 binds to IZUMO1 with an affinity higher than that required for initiating B cell activation and affinity maturation (31–34). The murine adaptive immune system can generate fertilization-inhibitory, anti-IZUMO1 antibodies against syngeneic sperm (Fig. 5*A*).

How does OBF13 interfere with sperm–egg interactions? We propose that OBF13 affects an allosteric interaction within IZUMO1 between the apex of the four-helix domain and the JUNO-binding site of the β-hairpin hinge region (Fig. 5*B*). We envision that IZUMO1 exists in an ensemble of conformations, predominantly populating structures in the boomerang conformation as suggested in the apo-structure (i.e., $K_1 < 1$). IZUMO1 molecules in the upright conformation have a higher affinity for JUNO ($K_3 > K_2$) and the upright confirmation is active for fertilization. Thermodynamics dictates that $K_1 K_3 = K_2 K_4$, so $K_4 > K_1$. Here, OBF13 leads to a higher proportion of IZUMO1 molecules in the boomerang conformation ($K_5 > 1$). Relative to the monomeric OBF13^{WT} scFv, the boomerang conformation is substantially stabilized through the oligomeric OBF13 IgM which has increased avidity or the monomeric OBF13^{HAC} scFv which has

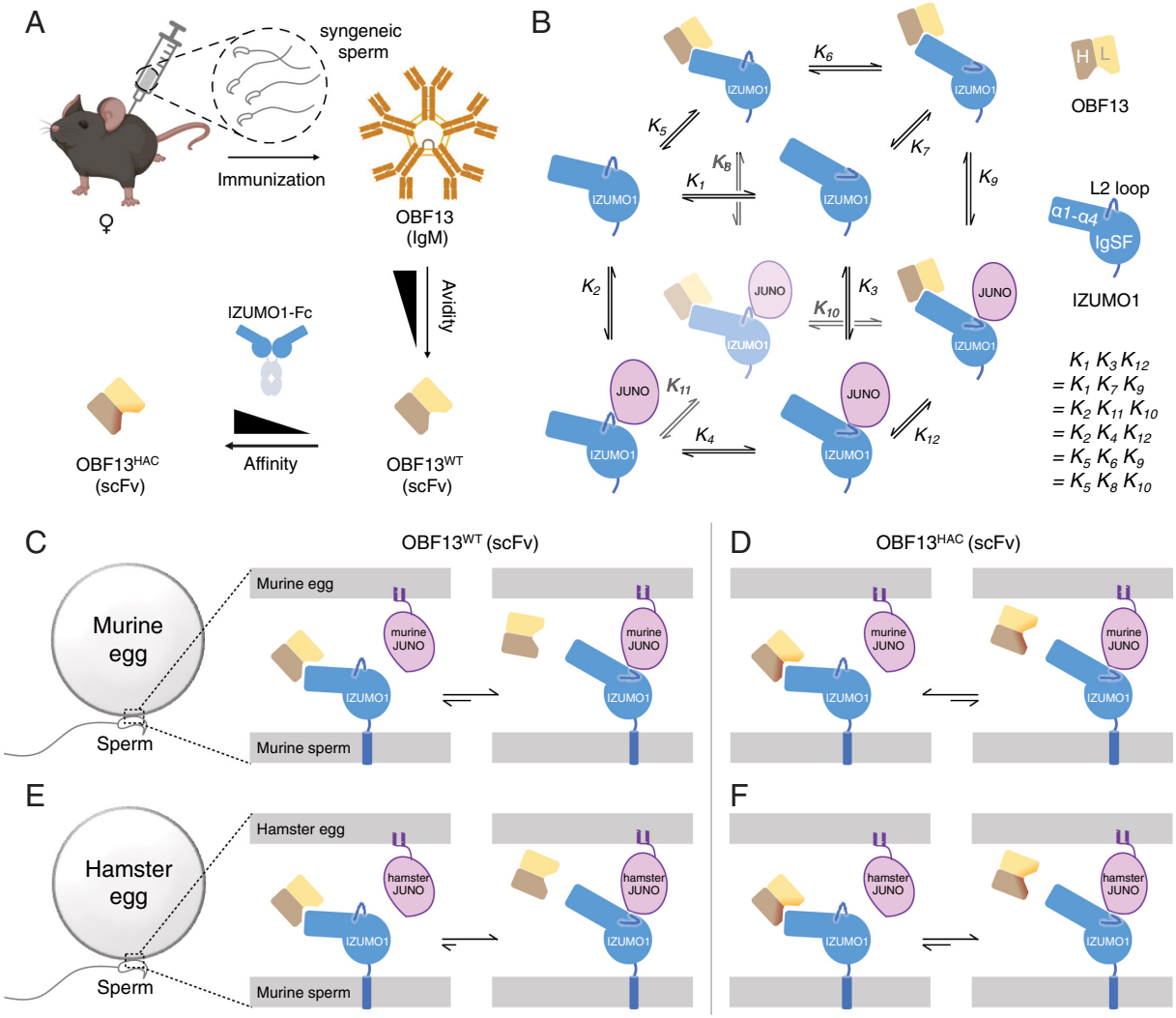

Fig. 5. Model of allosteric inhibition of IZUMO1 by OBF13. (*A*) A flowchart summarizes the discovery and engineering of OBF13. Relative to OBF13^{WT} (scFv), the decreased avidity of OBF13 (IgM) to IZUMO1 is offset by the increased affinity of OBF13^{HAC} (scFv). (*B*) A thermodynamic cycle for a ternary IZUMO1–OBF13–JUNO complex. For clarity, only two of the states in the conformational ensemble of apo-IZUMO1 (Upper-front) are depicted. In one of these states (*Left*), IZUMO1 adopts the boomerang shape, and the JUNO-binding surface is blocked by the L2 loop. In the second state (*Right*), the four-helix domain (α1-α4) has moved up and the L2 loop has moved down. OBF13 stabilizes IZUMO1 in the apo-conformation, thereby increasing the population of apo-IZUMO1 in the boomerang state and decreasing the population of apo-IZUMO1 in the JUNO-bound state. Equilibrium constants for each step in the thermodynamic cycle are indicated (*Discussion*). Cartoon schematics showing the effects of OBF13^{WT} (scFv) and OBF13^{HAC} (scFv) in the conformational equilibrium of IZUMO1 and the interactions between murine sperm's IZUMO1 and (*C* and *D*) murine egg's JUNO or (*E* and *F*) hamster egg's JUNO. Only the IZUMO1–JUNO interaction shown on the right side of the equilibrium is compatible with fertilization. For clarity, only one copy of IZUMO1 and JUNO and two conformations of IZUMO1 were shown.

increased affinity (increased K_5). Compared to IZUMO1 alone, the decreased association constant (k_{on}) for JUNO binding by the OBF13 IgM- or OBF13^{HAC} scFv-bound IZUMO1 ($K_{10} < K_4$) supports this model. These kinetic properties are consistent with a decreased fraction of OBF13-bound IZUMO1 molecules in the upright conformation ($K_7 < 1$, $K_3 > K_9$) (Fig. 5 *C* and *D*) (25, 35, 36). Previous hydrogen–deuterium exchange mass spectrometry of IZUMO1 (37) and molecular dynamics simulation of the IZUMO1–JUNO complex (38) support the notion of allostery.

Hamster JUNO leads to a higher proportion of IZUMO1 molecules in the upright conformation (increased K_4), compared to murine JUNO. $K_4\ K_{12} = K_{11}\ K_{10}$, so increased K_4 leads to increased K_{10}. Such enhancement is further potentiated by the avidity of JUNO on egg membranes. Despite the allosteric effect posed by OBF13, the resulting affinity remains sufficient for murine sperm adhering to hamster eggs for fertilization (Fig. 5 *E* and *F*). Using IZUMO1-Fc binding to membrane-bound JUNO as a proxy, the minimal EC_{50} value for successful fertilization by murine sperm is estimated to be in the range of 10 to 550 nM (Fig. 3*D*). These data provide a structural and mechanistic basis for antibody-mediated, species-specific inhibition of the IZUMO1–JUNO interaction in fertilization.

Evidence suggested that IZUMO1 is part of a large sperm membrane protein complex (39–41). Overlay of our crystal structure of IZUMO1–OBF13 with an AlphaFold model of the IZUMO1–SPACA6–TMEM81 complex (11, 12) showed that OBF13 and SPACA6 would clash if OBF13 were to bind IZUMO1 in its heterotrimeric state (Fig. 1*K*). This trimeric sperm complex was predicted by deep learning to interact with egg's JUNO and CD9, forming a hetero-pentameric complex at the fertilization synapse (11). Although we did not detect binding of IZUMO1 with CD9 (*SI Appendix*, Fig. S4*D*), in this model (Fig. 1*J*), OBF13 would additionally interfere with the contact between IZUMO1 and CD9 (Fig. 1*J*).

Alternatively, or in addition, IZUMO1 may play roles following sperm–egg binding. First, sperm–egg fusion may be accompanied by additional structural changes in IZUMO1's conformations or oligomeric states (42). OBF13 traps IZUMO1 in its apo-conformation,

potentially interfering with these subsequent changes. Second, the OBF13 epitope is immediately adjacent to the hydrophobic amino acid site (W113) of IZUMO1 previously identified in somatic cell–cell fusion (43). Should the four-helix domain of IZUMO1 interacts directly with the egg's plasma membranes, OBF13 would block these protein–membrane interactions.

The cocrystal structure of OBF13–IZUMO1 that we reported is, to our knowledge, the only structure of an antisperm antibody bound to its antigen to date. Several additional IZUMO1 monoclonal antibodies have been isolated and characterized as inhibitory to fertilization, many of which targeting epitopes within its four-helix domain (18, 42, 44). Reports of human IZUMO1 antibodies that recognize the four-helix domain in the sera of immuno-infertile patients suggest its immunogenicity in humans (45).

The identification of the fertilization-inhibitory epitope and the allosteric interaction within IZUMO1 sets the stage for the discovery and design of antisperm antibodies and immunocontraceptives. For example, the coupling between the apex of four-helix domain and the β-hairpin hinge in IZUMO1 could enable protein engineering efforts to induce the conformational changes of IZUMO1 (e.g., amino acid substitutions, insertions, and/or deletions in the four-helix domain). This coupling could therefore facilitate the design of contraceptive immunogens, the discovery of additional allosteric regulators of IZUMO1 activity, and high-throughput approaches to inhibitor discovery. The IZUMO1–OBF13 structure reported here will facilitate virtual drug screening to identify potential lead compounds (e.g., ref. 46). Specifically, we envision a small molecule binding to IZUMO1 contacting all or many of the residues of the OBF13 epitope in a conformation similar to that formed in the complex with OBF13 (Fig. 1 *D* and *E*). In addition, the structures of the indole and phenol rings and neighboring side chains of the OBF13 paratope (Fig. 2*A*) are potentially useful starting points for the design of fragment-based screening scaffolds (e.g., refs. 25 and 47). More broadly, our work has implications for advancing the understanding of naturally occurring antisperm antibodies and for developing immunocontraceptives that target sperm-surface antigens.

Materials and Methods

Additional information is provided in *SI Appendix, Materials and Methods*.

Protein Crystallization of IZUMO1–OBF13 and Apo-IZUMO1. The IZUMO1 ectodomain (residues 22–256) and OBF13 Fab were recombinantly expressed and purified from Expi293F cells. The IZUMO1–OBF13 (Fab) complex was crystallized at room temperature in hanging-drop vapor diffusion system. Then, 1 μL of the 11.1 mg/mL complex was mixed with 1 μL reservoir solution of 200 mM L-Proline, 100 mM HEPES pH 7.4, 9% PEG 3,350, over 1 mL of reservoir solution. The crystals were supplemented with PEG 400 before cryocooling in liquid nitrogen. Attempts to crystalize the IZUMO1–OBF13 (scFv) complex crystalized apo-IZUMO1 at room temperature in sitting-drop vapor diffusion system. Then, 400 nL of the 12.1 mg/mL IZUMO1 ectodomain (residues 22–256) and OBF13 (scFv)-His_6 was mixed with 400 nL of reservoir solution of 200 mM $CaCl_2$, 100 nM HEPES pH 7.5, 28% PPG P400, over 80 μL of reservoir solution. The crystals were supplemented with PEG 400 before cryocooling in liquid nitrogen.

In Vitro Fertilization of Murine Eggs by RBGS Murine Sperm. Cauda epididymal sperm from one RBGS transgenic male mouse, B6D2-Tg(CAG/Su9-DsRed2, Acr3-EGFP)RBGS002Osb, were preincubated at a density of 2×10^5 sperm/mL in Toyoda, Yokoyama, Hoshi (TYH) medium drops containing 1:50 dilutions of OBF13 antibodies at 37 °C, 5% CO_2 for 2 h. The cumulus cells and zonae pellucidae of eggs obtained from three B6D2F1/J female mice were removed by treating with 1 mg/mL collagenase in TYH at 37 °C for 10 min. Zona-free murine eggs were then transferred to the medium drops containing sperm and incubated for 30 min or 6 h to examine sperm binding or pronuclear formation, respectively. Sperm–egg complexes were fixed in 0.25% glutaraldehyde and stained with 1:1,000 dilution of Hoechst 33342 to visualize the nuclei. Z-stack images were captured under a Nikon Eclipse Ti microscope equipped with a Nikon C2 confocal module and the numbers of bound sperm and pronuclei in the eggs were counted under a Keyence BZ-X800 microscope.

Data, Materials, and Software Availability. The coordinates and structure factors of the IZUMO1–OBF13 complex and apo-IZUMO1 have been deposited in the RCSB Protein Data Bank (PDB) under assigned PDB IDs 9MYL (48) and 9MYM (49), respectively. All other data are included in the manuscript and/or *SI Appendix*.

ACKNOWLEDGMENTS. We thank Drs. Peter Kim, Polina Lishko, Masaru Okabe for discussion, and Dr. Daniel Fernandez of Stanford ChEM-H Macromolecular Structure Knowledge Center, and staff scientists of Stanford Synchrotron Radiation Lightsource (SSRL) beam lines 9-2 and 12-2 for X-ray crystallographic data collection. Use of the SSRL, SLAC National Accelerator Laboratory, is supported by the US Department of Energy (DOE), Office of Science, Office of Basic Energy Sciences under Contract DE-AC02-76SF00515. The SSRL Structural Molecular Biology Program is supported by the DOE Office of Biological and Environmental Research and by NIH NIGMS grant P41GM103393. Some figure panels were created with BioRender.com. This work was supported by an NIH NICHD grant R00HD104924 (S.T.), a David Sokal Innovation Award of Male Contraceptive Initiative 2024-303 (S.T.), the Ministry of Education, Culture, Sports, Science, and Technology/Japan Society for the Promotion of Science KAKENHI grants JP22K15103 (Y.L.), JP24K02033 (Y.L.), JP21H05033 (M.I.), and JP23K20043 (M.I.), a Japan Agency for Medical Research and Development grant JP23JF0126001 (M.I.), and a Takeda Science Foundation grant 2024032851 (Y.L.).

1. N. Inoue, M. Ikawa, A. Isotani, M. Okabe, The immunoglobulin superfamily protein Izumo is required for sperm to fuse with eggs. *Nature* **434**, 234–238 (2005).
2. E. Bianchi, B. Doe, D. Goulding, G. J. Wright, Juno is the egg Izumo receptor and is essential for mammalian fertilization. *Nature* **508**, 483–487 (2014).
3. D. Lorenzetti *et al.*, A transgenic insertion on mouse chromosome 17 inactivates a novel immunoglobulin superfamily gene potentially involved in sperm-egg fusion. *Mamm. Genome* **25**, 141–148 (2014).
4. T. Noda *et al.*, Sperm proteins SOF1, TMEM95, and SPACA6 are required for sperm-oocyte fusion in mice. *Proc. Natl. Acad. Sci. U.S.A.*, **117**, 11493–11502 (2020), 10.1073/pnas.1922650117.
5. I. Lamas-Toranzo *et al.*, TMEM95 is a sperm membrane protein essential for mammalian fertilization. *eLife* **9**, e53913 (2020).
6. S. Barbaux *et al.*, Sperm SPACA6 protein is required for mammalian sperm-egg adhesion/fusion. *Sci. Rep.* **10**, 5335 (2020).
7. T. Noda *et al.*, Sperm membrane proteins DCST1 and DCST2 are required for sperm-egg interaction in mice and fish. *Commun. Biol.* **5**, 332 (2022).
8. H. Pausch *et al.*, A nonsense mutation in TMEM95 encoding a nondescript transmembrane protein causes idiopathic male subfertility in cattle. *PLoS Genet.* **10**, e1004044 (2014).
9. S. Tang *et al.*, Human sperm TMEM95 binds eggs and facilitates membrane fusion. *Proc. Natl. Acad. Sci. U.S.A.* **119**, e2207805119 (2022).
10. N. Inoue, Y. Hagihara, I. Wada, Evolutionarily conserved sperm factors, DCST1 and DCST2, are required for gamete fusion. *eLife* **10**, e66313 (2021).
11. A. Elofsson, L. Han, E. Bianchi, G. J. Wright, L. Jovine, Deep learning insights into the architecture of the mammalian egg-sperm fusion synapse. *eLife* **13**, RP93131 (2024), 10.7554/eLife.93131.2.
12. V. E. Deneke *et al.*, A conserved fertilization complex bridges sperm and egg in vertebrates. *Cell* **187**, 7066–7078.e22 (2024), 10.1016/j.cell.2024.09.035.
13. M. Okabe, K. Takada, T. Adachi, Y. Kohama, T. Mimura, Inconsistent reactivity of an anti-sperm monoclonal antibody and its relationship to sperm capacitation. *J. Reprod. Immunol.* **9**, 67–70 (1986).
14. M. Okabe *et al.*, Capacitation-related changes in antigen distribution on mouse sperm heads and its relation to fertilization rate in vitro. *J. Reprod. Immunol.* **11**, 91–100 (1987).
15. Y. Kawai *et al.*, Flow cytometric analysis of mouse sperm using monoclonal anti-sperm antibody OBF13. *J. Reprod. Immunol.* **16**, 71–82 (1989).
16. M. Okabe *et al.*, Effect of a monoclonal anti-mouse sperm antibody (OBF13) on the interaction of mouse sperm with zona-free mouse and hamster eggs. *J. Reprod. Immunol.* **13**, 211–219 (1988).
17. M. Okabe *et al.*, An anti-mouse sperm monoclonal antibody (OBF13) and its inhibitory activity on fertilization. *Jpn. J. Fertil. Steril.* **33**, 473–478 (1988).
18. N. Inoue *et al.*, Molecular dissection of IZUMO1, a sperm protein essential for sperm-egg fusion. *Development* **140**, 3221–3229 (2013).
19. H. Aydin, A. Sultana, S. Li, A. Thavalingam, J. E. Lee, Molecular architecture of the human sperm IZUMO1 and egg JUNO fertilization complex. *Nature* **534**, 562–565 (2016).
20. U. Ohto *et al.*, Structure of IZUMO1–JUNO reveals sperm-oocyte recognition during mammalian fertilization. *Nature* **534**, 566–569 (2016).

21. K. Nishimura *et al.*, The structure of sperm Izumo1 reveals unexpected similarities with Plasmodium invasion proteins. *Curr. Biol.* **26**, R661–662 (2016).
22. J. D. Bloom, An experimentally determined evolutionary model dramatically improves phylogenetic fit. *Mol. Biol. Evol.* **31**, 1956–1978 (2014).
23. D. M. Fowler, S. Fields, Deep mutational scanning: A new style of protein science. *Nat. Methods* **11**, 801–807 (2014).
24. G. Chao *et al.*, Isolating and engineering human antibodies using yeast surface display. *Nat. Protoc.* **1**, 755–768 (2006).
25. S. Tang, P. S. Kim, A high-affinity human PD-1/PD-L2 complex informs avenues for small-molecule immune checkpoint drug discovery. *Proc. Natl. Acad. Sci. U.S.A.* **116**, 24500–24506 (2019).
26. N. Inoue, T. Saito, I. Wada, Unveiling a novel function of CD9 in surface compartmentalization of oocytes. *Development* **147**, dev189985 (2020).
27. T. Matsumura *et al.*, Sperm IZUMO1 is required for binding preceding fusion with oolemma in mice and rats. *Front Cell Dev. Biol.* **9**, 810118 (2021).
28. S. Oura *et al.*, Chimeric analysis with newly established EGFP/DsRed2-tagged ES cells identify HYDIN as essential for spermiogenesis in mice. *Exp. Anim.* **68**, 25–34 (2019).
29. E. Bianchi, G. J. Wright, Cross-species fertilization: The hamster egg receptor, Juno, binds the human sperm ligand, Izumo1. *Philos. Trans. R Soc. Lond. B Biol. Sci.* **370**, 20140101 (2015).
30. K. Kato *et al.*, Structural and functional insights into IZUMO1 recognition by JUNO in mammalian fertilization. *Nat. Commun.* **7**, 12198 (2016).
31. J. M. Dal Porto, A. M. Haberman, G. Kelsoe, M. J. Shlomchik, Very low affinity B cells form germinal centers, become memory B cells, and participate in secondary immune responses when higher affinity competition is reduced. *J. Exp. Med.* **195**, 1215–1221 (2002).
32. T. A. Shih, E. Meffre, M. Roederer, M. C. Nussenzweig, Role of BCR affinity in T cell dependent antibody responses in vivo. *Nat. Immunol.* **3**, 570–575 (2002).
33. H. N. Eisen, Affinity enhancement of antibodies: How low-affinity antibodies produced early in immune responses are followed by high-affinity antibodies later and in memory B-cell responses. *Cancer Immunol. Res.* **2**, 381–392 (2014).
34. R. K. Abbott *et al.*, Precursor frequency and affinity determine B cell competitive fitness in germinal centers, tested with germline-targeting HIV vaccine immunogens. *Immunity* **48**, 133–146.e136 (2018).
35. I. H. Moal, P. A. Bates, Kinetic rate constant prediction supports the conformational selection mechanism of protein binding. *PLoS Comput. Biol.* **8**, e1002351 (2012).
36. T. U. J. Bruun *et al.*, Structure-guided stabilization improves the ability of the HIV-1 gp41 hydrophobic pocket to elicit neutralizing antibodies. *J. Biol. Chem.* **299**, 103062 (2023).
37. T. D. R. Vance *et al.*, SPACA6 ectodomain structure reveals a conserved superfamily of gamete fusion-associated proteins. *Commun. Biol.* **5**, 984 (2022).
38. P. Pacak, C. Kluger, V. Vogel, Molecular dynamics of JUNO-IZUMO1 complexation suggests biologically relevant mechanisms in fertilization. *Sci. Rep.* **13**, 20342 (2023).
39. D. A. Ellerman *et al.*, Izumo is part of a multiprotein family whose members form large complexes on mammalian sperm. *Mol. Reprod Dev.* **76**, 1188–1199 (2009).
40. W. Contreras *et al.*, C11orf94/Frey is a key regulator for male fertility by controlling Izumo1 complex assembly. *Sci. Adv.* **8**, eabo6049 (2022).
41. Y. Lu *et al.*, 1700029I15Rik orchestrates the biosynthesis of acrosomal membrane proteins required for sperm-egg interaction. *Proc. Natl. Acad. Sci. U.S.A.* **120**, e2207263120 (2023).
42. N. Inoue, Y. Hagihara, D. Wright, T. Suzuki, I. Wada, Oocyte-triggered dimerization of sperm IZUMO1 promotes sperm-egg fusion in mice. *Nat. Commun.* **6**, 8858 (2015).
43. N. G. Brukman *et al.*, A novel function for the sperm adhesion protein IZUMO1 in cell-cell fusion. *J. Cell Biol.* **222**, e202207147 (2023).
44. N. Miyazaki *et al.*, Isolation and characterization of antigen-specific alpaca (Lama pacos) VHH antibodies by biopanning followed by high-throughput sequencing. *J. Biochem.* **158**, 205–215 (2015).
45. S. Clark, R. K. Naz, Presence and incidence of izumo antibodies in sera of immunoinfertile women and men. *Am. J. Reprod. Immunol.* **69**, 256–263 (2013).
46. J. Lyu *et al.*, Ultra-large library docking for discovering new chemotypes. *Nature* **566**, 224–229 (2019).
47. D. A. Erlanson, S. W. Fesik, R. E. Hubbard, W. Jahnke, H. Jhoti, Twenty years on: The impact of fragments on drug discovery. *Nat. Rev. Drug Discov.* **15**, 605–619 (2016).
48. S. Tang, Fertilization IZUMO1 protein ectodomain in complex with anti-sperm antibody OBF13. RCSB Protein Data Bank. http://www.rcsb.org/pdb/explore/explore.do?structureId=9MYL. Deposited 22 January 2025.
49. S. Tang, Fertilization IZUMO1 protein ectodomain. RCSB Protein Data Bank. http://www.rcsb.org/pdb/explore/explore.do?structureId=9MYM. Deposited 22 January 2025.